Cite this article
Bahmanpouri F, Gualtieri C and Chanson H
Flow patterns and free-surface dynamics in hydraulic jump on pebbled rough bed.
Proceedings of the Institution of Civil Engineers – Water Management,
https://doi.org/10.1680/jwama.20.00040

Research Article
Paper 2000040
Received 24/04/2020;
Accepted 09/03/2021

Keywords: fluid mechanics/hydraulics & hydrodynamics/river engineering

Water Management

ice Publishing

Flow patterns and free-surface dynamics in hydraulic jump on pebbled rough bed

1 Farhad Bahmanpouri PhD
Civil, Architectural and Environmental Engineering Department (DICEA), University of Napoli Federico II, Napoli, Italy (Orcid:0000-0001-7037-3548) (corresponding author: farhad.bahmanpouri@unina.it)

2 Carlo Gualtieri
Professor, Civil, Architectural and Environmental Engineering Department (DICEA), University of Napoli Federico II, Napoli, Italy (Orcid:0000-0002-3717-1618)

3 Hubert Chanson
Professor, School of Civil Engineering, The University of Queensland, Brisbane QLD, Australia (Orcid:0000-0002-2016-9650)



Some basic characteristics of a classic hydraulic jump flow over a pebbled rough bed, as well as on a smooth bed as a reference, are presented in this experimental study. For the experiments, an inflow Froude number Fr_1 from 1.54 to 4.94 and inflow Reynolds number Re_1 from 42 000 to 230 000 were considered. Visual observations and measurements suggested some differences between the formation of a hydraulic jump on rough and smooth bed configurations, including different air entrainment processes, larger vortical structures in the roller length and stronger backward flow in the upper layer. Furthermore, the jump roller and aerated flow lengths were shorter on a pebbled rough bed than on a smooth bed, while the dimensionless advection velocity of large vortices was the same for both bed types. The instantaneous jump toe perimeter showed the largest variation at the largest Fr_1 and was generally larger on rough bed than on smooth bed. Larger oscillations of the free-surface profile were observed on smooth bed, highlighting that roughness resulted in smaller free-surface oscillations, suggesting the higher rate of energy dissipation.

Notation

C	time-averaged void fraction defined as volume of air per unit volume of air and water
d_1	inflow water depth (m) immediately upstream of the jump toe
d_2	downstream water depth (m)
d_{50}	median particle size of a distribution (m)
d_c	critical depth (m)
F	bubble count rate defined as the number of bubbles or water droplets per second (Hz)
F_{eddy}	characteristic frequency of formation and downstream ejection of the large vortices in the shear layer (Hz)
Fr_1	inflow Froude number: $Fr_1 = V_1/(g \times d_1)^{1/2}$
F_{toe}	characteristic frequency (Hz) of longitudinal oscillations of jump toe position
f	Darcy–Weisbach friction coefficient
g	gravitational acceleration (m/s^2): $g = 9.80$ m/s^2 in Brisbane, Australia
h	upstream gate opening (m)
K_s	roughness coefficient (m)
L_{air}	length of the bubbly flow region (m)
L_r	jump roller length (m)
Q	flow rate (m^3/s)
Re^*	shear Reynolds number: $Re^* = K_s \times u^*/\upsilon$
Re_1	inflow Reynolds number: $Re_1 = \rho \times V_1 \times d_1/\mu$
St	Strouhal number: $St = F_{toe}\, d_1/V_1$
U_{eddy}	advection velocity (m/s) of large-scale vortices in the jump roller
u^*	shear velocity (m/s) ($u^* = V_1 \times (f/8)^{0.5}$)
V	air–water interfacial velocity (m/s)
V_1	average inflow velocity (m/s): $V_1 = Q/(W \times d_1)$
W	channel width (m)
x	longitudinal distance (m) from the upstream sluice gate
x_1	longitudinal position (m) of jump toe
x_{toe}	longitudinal position of jump toe (m)
x'_{toe}	standard deviation of the instantaneous jump toe position (m)
y	vertical distance (m) above the channel bed
z	transversal distance (m) from the channel centreline
$\Delta(\eta/d_1)$	range of variation for water surface
η	water elevation above the channel bed (m)
η'	standard deviation of the instantaneous water elevation (m) above the channel bed
μ	dynamic viscosity (Pa s)
ρ	density (kg/m^3)
ρ_s	gravel density (kg/m^3)
υ	kinematic viscosity (m^2/s)
Ø	diameter (m)

1. Introduction

A hydraulic jump is a sudden transition from upstream supercritical to downstream subcritical flow which is associated with air entrainment, energy dissipation, spray, surface splashing and waves (Chanson, 2004). The three-dimensional structure of a hydraulic jump is extremely complex (Chanson, 2009; Lennon and Hill, 2006), and is not yet fully understood (Chanson, 2010; Rajaratnam, 1967). The study of the hydraulic jump dates back some time, to the first observation by Leonardo Da Vinci (Montes, 1998) and the experimental and theoretical research of Bidone (1820), as this phenomenon has been very extensively investigated in river and hydraulic engineering. On a smooth bed, Rao and Kobus (1971) reported early laboratory studies on hydraulic jump properties. Further relevant studies identified free-surface dynamics (Bayon *et al.*, 2016, Mouaze *et al.*, 2005) air entrainment (Murzyn and Chanson, 2009; Takahashi and Ohtsu, 2017), air bubble clustering (Felder and Pfister, 2017; Gualtieri and Chanson, 2010, 2013; Wang, 2014; Witt *et al.*, 2018) and turbulence properties (Mortazavi *et al.*, 2016, Wang and Chanson, 2015, 2016) on a smooth bed.

A bed is considered to be smooth or rough if Re* is lower than 5 or larger than 50, respectively, where Re* is defined as the shear Reynolds number $\mathrm{Re}^* = K_s \times u^*/\upsilon$, with u^* as shear velocity ($u^* = V_1 \times (f/8)^{0.5}$), wherein V_1 is inflow velocity and f is the Darcy friction factor; K_s is the roughness coefficient and υ is the kinematic viscosity (Chanson, 2004). Polyvinyl chloride (PVC), with K_s about 0.5 mm, is generally a smooth bed. Table 1 lists the literature studies on hydraulic jump on rough bed with the main parameters. However, studies about the hydraulic jump in channels covered with uniform gravel, which is very frequent in natural channels, are lacking. This paper presents the results of a novel experimental study where the basic findings on such a bed, including flow patterns, jump toe oscillation and water surface profile, were investigated. The present research has some implications for hydraulic and environmental engineering design, because most hydraulic structures, stormwater and water treatment systems are operating at inflow Reynolds numbers larger than 10×10^5. Furthermore, in natural channels, almost all flows are hydraulically rough.

The aim of the study is to evaluate comparatively the effect of roughness on the above features of the hydraulic jump. Hence, basic flow patterns are analysed using photographs taken during the experiments. Second, the observations and results in terms of basic parameters, including conjugate depth relationship and jump roller and aerated flow length, are presented and discussed. Third, the oscillations of jump toe position, recorded with a high-speed camera, are analysed. Finally, the transverse perimeter of the hydraulic jump toe, as well as free-surface dynamics, are reported and discussed. Boundary friction force, shear stress and vortex advection velocity are presented in Appendix 1.

2. Dimensional analysis and experimental set-up

2.1 Dimensional analysis

For a hydraulic jump in a horizontal, rectangular channel, dimensional considerations result in a series of dimensionless relationships in terms of the turbulent air–water flow properties at a position (x, y, z) within the hydraulic jump, as functions of the fluid properties and boundary conditions. Assuming the upstream flow depth d_1 as the characteristic length scale, a simplified dimensional analysis yields (Chanson, 2005):

$$\frac{\eta}{d_1}, \frac{\eta'}{d_1}, \frac{(x_{toe} - x_1)}{d_1}, \frac{(x'_{toe})}{d_1}, \frac{F_{toe} \times d_1}{V_1}, \frac{F_{eddy} \times d_1}{V_1}, C, \frac{F \times d_1}{V_1}, \frac{V}{V_1}, \frac{U_{eddy}}{V_1} = F\left(\frac{x - x_1}{d_1}, \frac{x_1}{d_1}, \frac{W}{d_1}, \frac{K_s}{d_1}, \mathrm{Fr}_1, \mathrm{Re}\right) \quad (1)$$

where η is the water elevation above the channel bed (m); η' is the standard deviation of the instantaneous water elevation (m) above the channel bed; x_{toe} is the longitudinal position of jump toe (m); x'_{toe} is the standard deviation of the instantaneous jump toe position (m); F_{eddy} is the characteristic frequency of formation and downstream ejection of the large vortices in the shear layer (Hz); U_{eddy} is the advection velocity (m/s) of large-scale vortices in the jump roller; F_{toe} is the characteristic frequency (Hz) of longitudinal oscillations of jump toe position; d_1 is the inflow water depth (m) immediately upstream of the jump toe; C is the time-averaged void fraction defined as volume of air per unit volume of air and water; F is the bubble count rate defined as the number of bubbles or water droplets per second (Hz); V is the air–water interfacial velocity (m/s); V_1 is the average inflow velocity (m/s): $V_1 = Q/(W \times d_1)$; K_s is the roughness coefficient (m); x is the longitudinal distance (m) from the upstream sluice gate; y is the vertical distance (m) above the channel bed; z is the transversal distance (m) from the channel centreline; W is the channel width (m); x_1 is the longitudinal position (m) of the jump toe

Equation 1 highlights the most essential variables for the physical modelling of a classical hydraulic jump based on the upstream flow depth d_1 as a characteristic length scale.

2.2 Experimental set-up

The experimental tests were carried out in the Hydraulic Laboratory at the University of Queensland, Australia. The rectangular flume was 3.2 m long, 0.5 m wide and 0.41 m high. The material of the side-wall was glass, while the bed material was high-density polyethylene (HDPE). A semi-circular edge ($Ø = 0.3$ m) was used in the upstream gate to remove the contraction of flow (Figure 1). The longitudinal position of the jump toe was selected at $x_1 = 1$ m. An overshoot gate at the downstream end was used to control the jump toe position. A Venturi meter was applied to measure the flow rate with an accuracy of ±2%. To record videos with a high-speed video-photography camera Casio Ex-10 Exilim

Table 1. Summary of literature review of hydraulic jump based on rough bed condition

Reference	Flume dimension: cm	Roughness type (K_s: mm)	K_s/d_1	Fr_1	Re_1	Discharge rate: m^3/s	Instrumentation
Hughes and Flack (1984)	FL = 213 FW = 30.5 FH = – FS = 0.0	■ Two strip roughness beds (K_s: 4.4–6.4) ■ Three densely packed gravel beds (K_s: 6.4–11.3)	0.1–1.4	3.44–8.04 2.34–10.5	—	0.010–0.015	■ Piezometers for measuring tailwater depth ■ Pitot-static tube for measuring velocity ■ Point gauge
Defina *et al.* (2008)	FL = 200 FW = 38 FH = 50 FS = 0.04	■ Spherical pebbles of ball-clay (K_s: 6.7)	—	1.9–10.57	0.5×10^5– 1×10^5	—	■ Magnetic flowmeter for measuring discharge
Pagliara *et al.* (2008)	FL = 600 FW = 35 FH = 50 FS = 0.0	■ Homogeneous ■ and non-homogeneous sediments, gravel (K_s: 6.26–45.6)	0.13–3.13	2.2–12.2	21 000–110 000	0.006–0.031	■ Magnetic flowmeter for measuring discharge ■ Digital video recording for measuring depths
Carollo *et al.* (2013)	FL = 490 FW = 30.4 FH = 24 Angle = 8.5,12,17.5	■ Crushed angular elements (K_s = 54)	—	1.76–6.11	—	—	■ Electro-magnetic flow meter for measuring discharge ■ Point gauge
Pagliara and Palermo (2015)	Channel 1: FL = 600 FW = 34.5 FH = 50 FS = –0.05	Gravel (K_s: 6.26–30.62)	0.13–3.13	2–9.5	—	—	■ Point gauge for measuring flow depth ■ Air-flow properties were measured using a USBR single- ■ tip conductivity probe air concentration meter
Felder and Chanson (2016, 2018)	FL = 320 FW = 50 FH = 41 FS = 0.0	■ Two different ■ rubber mats ■ A: K_s: 12 ■ B: K_s: 39	0.18– 1.1	1.5–6.5 1.7–4.6	2.3×10^4– 2.1×10^5 6.3×10^4– 2.1×10^5	0.012–0.103 0.032–0.106	■ Two double-tip conductivity probe systems for measuring air entrainment properties (tip Ø = 0.0125 and 0.25 mm) ■ Pointer gauge ■ Digital cameras ■ High- speed video capabilities

FL, flume length; FW, flume width; FH, flume height; FS, flume slope

camera (240 frames per second in high-speed mode with the resolution of 512×384 pixels), some light-emitting diode light projectors were used. The details of experimental runs including the inflow conditions are listed in Table 2.

Natural river pebbles with $d_{50} = 0.01135$ m, average density $\rho_s = 2.53$ g/cm^3 and particle size in the range 9.5–13.2 mm (previously used by Li and Chanson (2018)) were used as bed material. Note that the present data with $K_s = 1.13$ cm and $f = 0.051$–0.052 resulted in $900 < Re^* < 2400$. To achieve a uniform channel bed roughness, the gravels were installed on the whole length of the channel, including upstream of and underneath the upstream sluice gate. The gravels were fixed on wooden boards using tile adhesive (Dunlop, trade resaflex), and the boards were installed on the channel HDPE bed from upstream to downstream covering the whole length of the channel, including beneath the upstream sluice gate and in the upstream reservoir (Figure 2). To prevent the uplift of the boards, two (polymethyl methacrylate) walls were fixed to the boards on both sides of the flume. This set-up decreased the channel width to 0.475 m. More details of the rough bed preparation are described in Bahmanpouri *et al.* (2019).

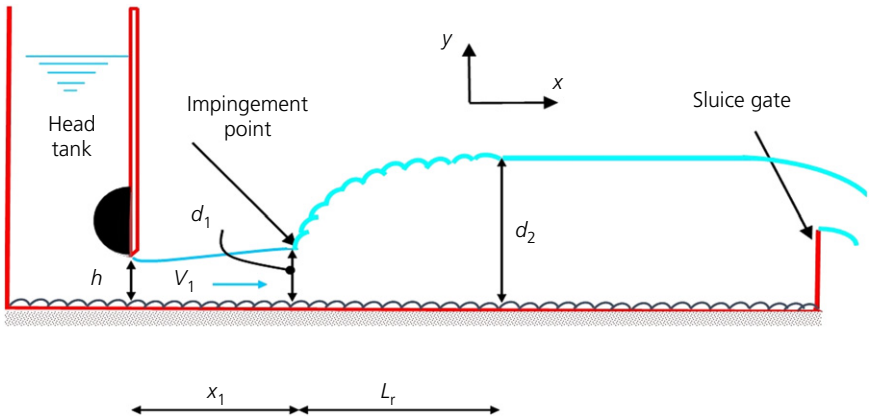

Figure 1. Definition sketch of experimental set-up. x_1 is longitudinal jump toe position; L_r is jump roller length; h is upstream gate opening; d_1 is inflow depth; V_1 is cross-sectional average inflow velocity; d_2 is downstream depth

Table 2. Details of flow conditions for the experimental runs in the current study with $x_1 = 1$ m

Experiment	Bed type	h_1: m	Q: m^3/s	d_1: m	Fr_1	Re_1	Comment
Present study	Smooth	0.03	0.02–0.044	0.031–0.0325	2.17–4.94	4.2×10^4–9.5×10^4	High-video-speed camera,
		0.06	0.036–0.095	0.06–0.063	1.54–3.93	7.8×10^4–2.0×10^5	240 frames/s
	Rough	0.06	0.042–0.1	0.078–0.085	1.31–2.87	9.6×10^4–2.3×10^5	Point gauge

3. Basic properties of hydraulic jump

3.1 Flow patterns by visual observation

According to the inflow Froude number Fr_1 ($Fr_1 = V_1/(g \times d_1)^{0.5}$), different types of jumps can be defined as: (*a*) undular jumps with no air entrainment; (*b*) undular jumps consisting of small air bubbles; (*c*) classic hydraulic jumps consisting of small roller length and surface waves; and (*d*) classic hydraulic jumps with detectable roller length (Chanson, 2004). For $Fr_1 < 1.5$, undular hydraulic jumps without air bubbles were observed associated with unstable undulations, transverse and longitudinal oscillations and small ripples at the free-surface area. Standing waves with some troughs and peaks were observed at the middle of the undular jump as in undular hydraulic jump on uniform bed roughness for $Fr_1 < 2.2$ (Felder and Chanson, 2016, 2018). For $1.5 < Fr_1 < 2.1$, for a rough bed condition, undular hydraulic jumps with air entrainment were seen, whereas, for a smooth bed, no undulations were observed but the jump roller appeared. Air bubbles were entrapped at the first undular wave crest and then advected toward the free surface.

Figure 2. Installed gravels on the channel bed

As Fr_1 increased, for $2.1 < Fr_1 < 2.5$ on a rough bed, a stronger rate of air entrainment associated with large eddies in the turbulent shear layer was observed. The unstable jump roller led to the formation of secondary undulations in the surface further downstream (Figures 3(a) and 3(b)). Furthermore, a recirculating flow was observed from the first wave crest (Figure 3(b)), while, in the clear water region near the bed, air bubbles were periodically observed to shed into the clear water core region. Herein, the interaction between the vortex shedding and the boundary layer resulted in the formation and development of large-scale eddies, which were advected downstream.

For $2.5 < Fr_1 < 3.1$, on both configurations, hydraulic jump with marked roller length and substantial turbulence was observed (Figure 3(c)), as already reported for a smooth bed (Chachereau

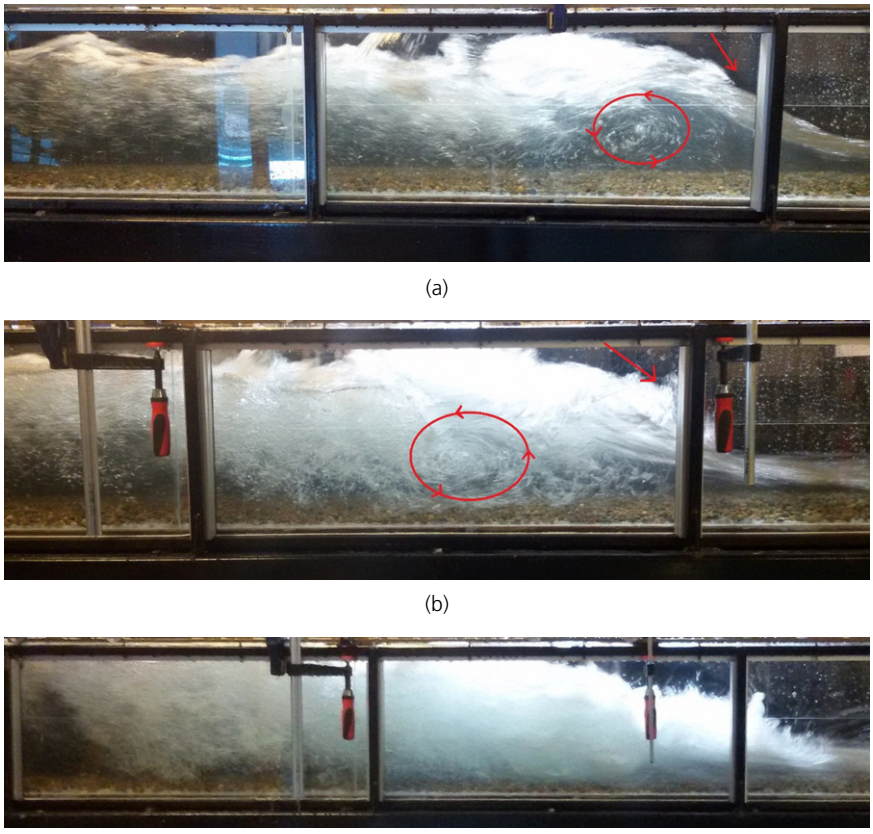

Figure 3. Hydraulic jump on rough bed; undular jump with unstable roller ($h = 0.06$ m). 'Circular arrow shows formation ofthe vortex; straight arrow shows negative flow : (a) flow condition: $Q = 0.076$ m^3/s, $Fr_1 = 2.07$, flow from right to left; (b) flow condition: $Q = 0.085$ m^3/s,$Fr_1 = 2.4$, flow from right to left; (c) flow condition: $Q = 0.1$ m^3/s, $Fr_1 = 2.87$, flow from right to left

and Chanson, 2011; Hoyt and Sellin, 1989; Wang *et al.*, 2015). On the rough bed, large vortical structures caused some irregular surface fluctuations, and in the recirculation zone a strong backward flow was observed. These features were probably related to the greater rate of energy dissipation on the rough bed. It is worth noting that different types of roughness result in additional resistance and hence lead to increasing the rate of energy dissipation (Carollo *et al.*, 2007; Defina *et al.*, 2008; Pagliara *et al.*, 2011). As investigated by the authors, comparisons between the rough and smooth bed configurations highlighted that the larger interactions between the shear layer and rough bed resulted in the formation of larger eddies with a high rate of turbulent intensity causing a large rate of energy dissipation. Furthermore, the rate of energy dissipation showed a direct relationship with the roughness coefficient and inflow Froude number (Felder and Chanson, 2018).

3.2 Conjugate depth relationship

Measurements of water depth using a pointer gauge were recorded for several seconds and averaged (Bahmanpouri, 2019). The upstream supercritical depth was measured at the position of $x_1 = 0.9$ m while the downstream subcritical depth was recorded at the end point of the jump roller. The upstream sluice gate opening was adjusted using a ruler on top of the gravels to achieve the average height. Water depth measurements using a point gauge were recorded based on the average height above the gravels, as was done for the gate opening.

A theoretical relationship between the conjugate depths d_1 and d_2 can be derived from the momentum equation as

$$2. \quad d_2/d_1 = 0.5 \times (\sqrt{1 + 8 \times Fr_1^2} - 1)$$

which is the Bélanger equation as defined by Bélanger (1841), which was derived under the following assumptions:

(*a*) the channel was rectangular and horizontal
(*b*) at the conjugate depths, the distribution of velocity was uniform and the distribution of pressure was hydrostatic
(*c*) there was no friction – that is, the boundary channel resistance was negligibly small compared to other forces.

Two empirical equations were proposed in the literature on rough beds to relate d_2/d_1 to Fr_1 and K_s. Carollo *et al.* (2009)

from their data collected on a gravel bed with different relative roughness height, from $0.33 < K_s/d_1 < 1.25$ proposed

3. $$\frac{d_2}{d_1} = 1 + \sqrt{2}\exp\left(\frac{-K_s}{d_c}\right)(\mathrm{Fr}_1 - 1)^{0.963}$$

where $K_s = d_{50}$ and d_c is critical depth, defined as $d_c = (q^2/g)^{1/3}$. Ead and Rajaratnam (2002) referring to a corrugated bed proposed

4. $$\frac{d_2}{d_1} = \mathrm{Fr}_1$$

The data from the present study and those from previous studies on smooth beds (Chachereau and Chanson, 2011; Kucukali and Chanson, 2008; Murzyn *et al.*, 2007; Wang, 2014) and on rough beds (Carollo *et al.*, 2007; Hughes and Flack, 1984), as well as Equations 2–4, are compared in Figure 4.

The present data on the smooth bed were well aligned and generally in agreement with the literature data (Figure 4(a)). On the rough bed, the comparative analysis showed a scatter among all the experimental data. The data from Carollo *et al.* (2007) were divided in five groups having K_s/d_1 in the range from 0.08 to 0.80. These data showed that the conjugate depth ratio decreased as the dimensionless roughness K_s/d_1 increased (Figure 4(b)). Furthermore, the data with $K_s/d_1 < 0.19$ were generally aligned with the Bélanger equation (Figure 4(b)). Figure 4(c) compares the data from the present study ($0.13 < K_s/d_1 < 0.14$) with those from Carollo *et al.* (2007) and Hughes and Flack (1984) having a similar dimensionless roughness – that is, $K_s/d_1 < 0.19$. At the end, the present data were generally aligned with those literature data, but some data from the present study were considered as suspicious and removed from the further analysis.

It should also be noted that due to the large vertical oscillations of the free surface and water splashing near the surface, the measurement of inflow depth is affected by uncertainties, which Wang estimated as up to ±8% (Wang, 2014). Furthermore, the exact definition of upstream depth d_1 can affect the conjugate depth relationship, especially in terms of (*a*) free-surface recording with the pointer gauge and (*b*) position of the zero-bed elevation defined on rough beds (Felder and Chanson, 2018).

3.3 Jump roller and aerated flow lengths

The jump roller length L_r is defined as the distance starting from the toe of the jump to the end section of the roller (Murzyn and Chanson, 2009). Herein, L_r was derived from the observed mean free-surface profiles from the side view as the distance starting from the toe of the jump to the end section of the roller (Figure 1). A comparative analysis of the dimensionless roller length L_r/d_1 based on Fr_1 is shown in Figure 5. Hager *et al.* (1990) proposed a correlation for the roller length on a smooth bed

5. $$\frac{L_r}{d_1} = 6 \times (\mathrm{Fr}_1 - 1)$$

Equation 5 was herein modified using the present data and those from Carollo *et al.* (2009) to include roughness height as

6. $$\frac{L_r}{d_1} = 6 \times (\mathrm{Fr}_1 - 1)^{[1-0.64\times(K_s/d_1)]} \quad 1 < \mathrm{Fr}_1 < 5$$

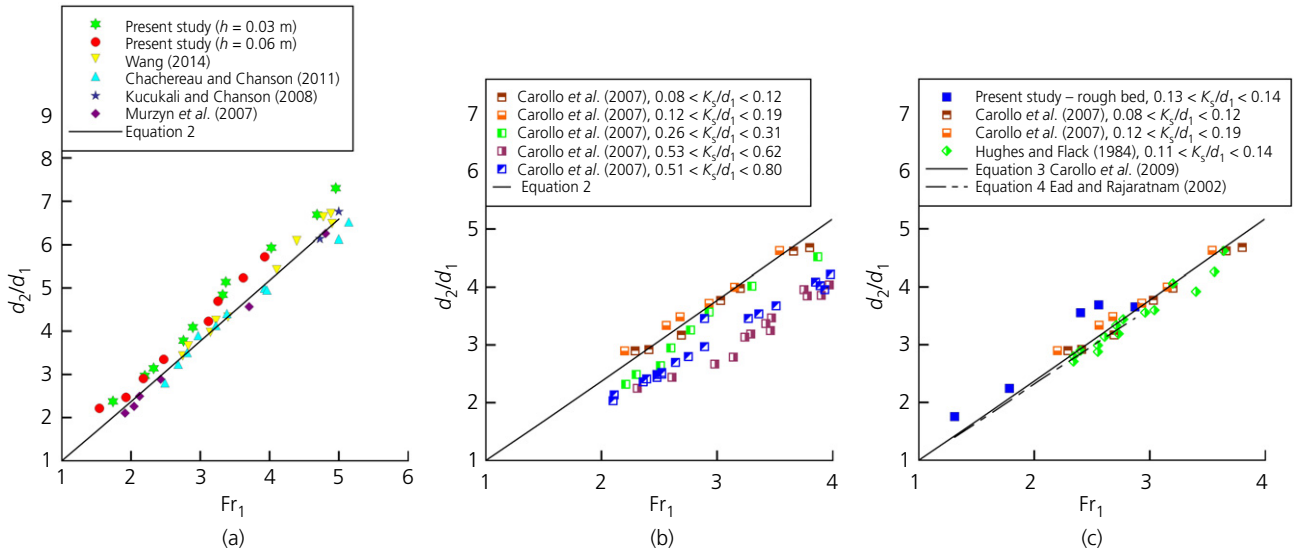

Figure 4. Conjugate depth ratio d_2/d_1: (a) smooth bed; (b) rough bed, all data; (c) rough bed with the similar K_s

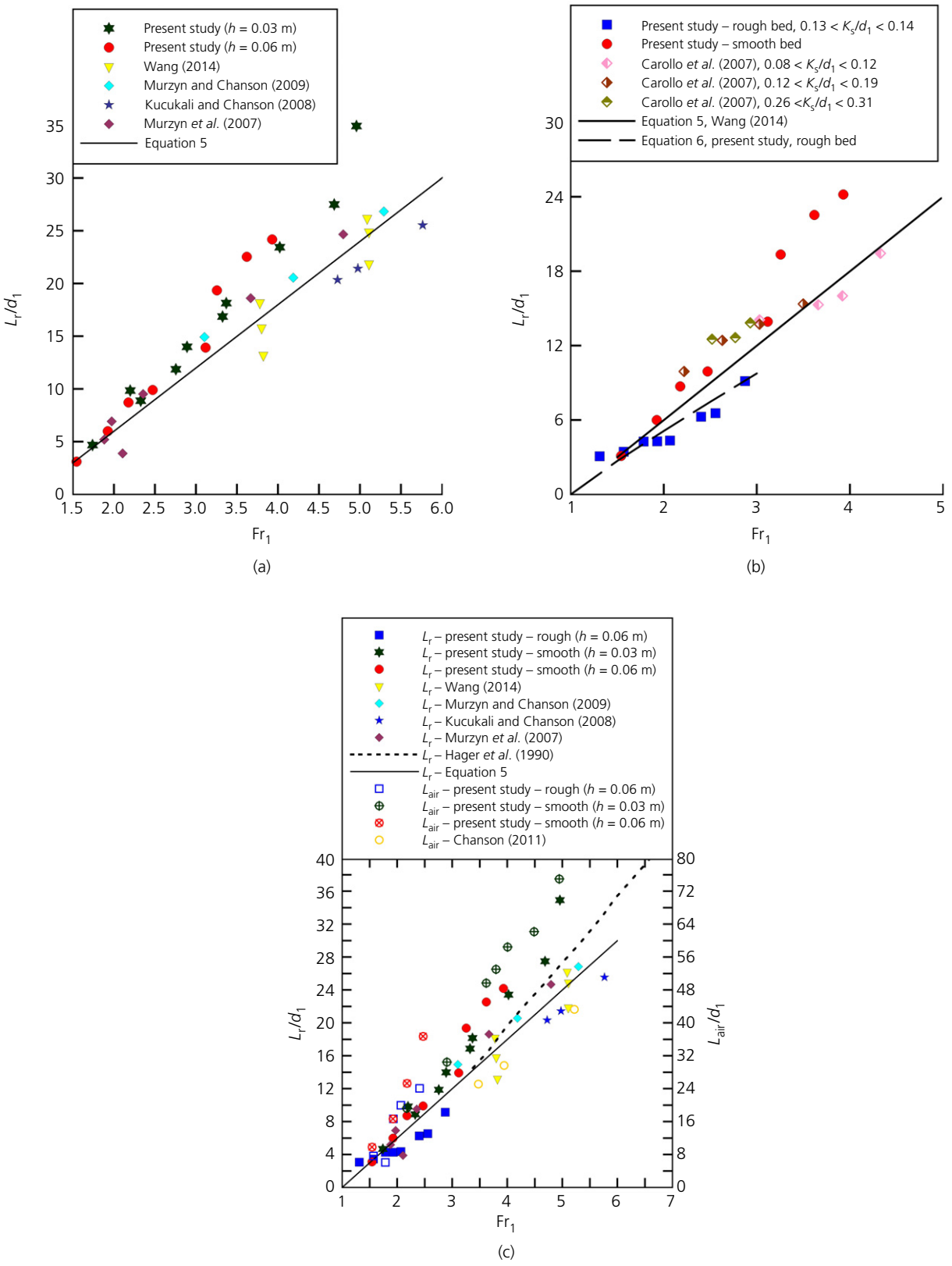

Figure 5. Jump roller length: (a) smooth bed; (b) rough bed; (c) relationship between dimensionless air-flow length and jump roller length

Equation 6 yielded $R = 0.95$ and standard error, SE = 0.7 and $R = 0.98$ and SE = 1.47 on rough and smooth bed, respectively. L_r/d_1 on pebbled rough bed was shorter than that on smooth bed (Figure 5(b)), suggesting a larger level of energy dissipation on the rough bed.

The length of the bubbly flow region L_{air} was measured from the entrained air bubbles observed through the side-wall downstream. Thus, L_{air} was considered as the average length of the bubbly flow. The present data were compared with those by Chanson (2011) on smooth bed (Figure 5(c)). The observed differences could be due to a different method of detecting the last bubbles at the end point, where the bubbles disappear. On smooth bed, L_{air} was comparatively longer at the larger h and Re_1, while, at the same h and Fr_1, the aerated flow and the jump roller on rough bed were shorter than those on smooth bed (Figure 5(c)). It is worth mentioning that the hydraulic jump parameters including sequent depth ratio, air flow length and roller length are dependent upon the inflow Froude number, Reynolds number and inflow aspect ratio (Hager and Bremen, 1989). As the present study was conducted based on a constant channel width, therefore, further investigations of hydraulic jump properties in terms of different inflow aspect ratios might be relevant.

4. Dynamics of impingement perimeter and free-surface profile

4.1 Oscillations of the jump toe position

Depending upon the inflow conditions, the hydraulic jump shifted its toe position about the mean longitudinal position x_1, in both slow- and fast-changing manners. The fast oscillations of the jump toe have already been investigated by Long *et al.* (1991), Gualtieri and Chanson (2007) and Wang (2014), and related to the development of large vortical structures in the roller length and their advection downstream through the shear layer. Gualtieri and Chanson (2007) studied the oscillation of the jump toe in terms of Strouhal number ($St = F_{toe} \times d_1/V_1$) and reported a range from 0.005 to 0.5 at an Fr_1 from 5.2 to 14.3.

Herein, the oscillations of the longitudinal position of the jump toe followed a pseudo-periodic manner. F_{toe} and F_{eddy} were calculated from the analysis of video frames recorded from the up and side view, respectively. In this regard, the number of jump toe oscillation and vortex ejections according to time was considered as the frequency of jump toe oscillation and vortex ejection, respectively. Based on visual observations, some interactions between the characteristics of the two-phase flow could be suggested. First, the formation of the vortex was associated with the instantaneous downstream movement of the jump toe, and second, the largest longitudinal shift of the jump toe position occurred once the vortex detached from the impingement point, as already reported by Wang (2014). Simultaneously, as the jump toe moved upstream, the detached vortex was advected longitudinally toward the downstream. Both motions could be related to the air entrainment at the impingement of the jump toe. The analysis of the oscillations was conducted in terms of two characteristic dimensionless frequencies, the dimensionless oscillation, that is, $F_{toe} \times d_1/V_1$, and the vortex ejection frequency, that is, $F_{eddy} \times d_1/V_1$ (Table 3).

Table 3. Characteristic frequency of jump toe oscillation and vortex production

	All flow conditions		$2.2 < Fr_1 < 3.0$	
Bed type	F_{toe}: Hz	F_{eddy}: Hz	$F_{toe} \times d_1/V_1$	$F_{eddy} \times d_1/V_1$
Smooth bed	0.4–0.9	0.6–1.0	0.014–0.022	0.019–0.02
Rough bed	0.5–0.7	0.5–0.6	0.021–0.023	0.019–0.02

Wang (2014) found that, on a smooth bed, these frequencies were related to the inflow Froude number Fr_1 as

$$\frac{F_{toe} \times d_1}{V_1} = 0.054 \times \exp(-0.33 \times Fr_1) \quad 2.8 < Fr_1 < 7.1 \tag{7}$$

$$\frac{F_{eddy} \times d_1}{V_1} = 0.034 \times \exp(-0.26 \times Fr_1) \quad 2.8 < Fr_1 < 7.1 \tag{8}$$

On rough bed, the dimensionless oscillations were slightly larger than those on smooth bed (Figure 6), due probably to the large vortices associated with the gravel bed. Furthermore, $F_{toe} \times d_1/V_1$ decreased as Fr_1 increased.

Within the roller, the vortex ejection frequency decreased as Fr_1 increased on both rough and smooth beds, although the observations were sometimes difficult due to the rapid pairing and merging of two successive eddies. It is worth pointing out that, once eddies were advected further downstream, they tended to break up. (Figure 7).

The data suggested that the dimensionless frequencies, F_{toe} and F_{eddy}, were observed to decrease as Fr_1 increased, on both bed types (Figures 6 and 7). This trend was consistent with those of past studies. The observed characteristic frequency of jump toe oscillation F_{toe} and vortex production F_{eddy} were comparable. For $Fr_1 > 2.0$, large vortices appeared (Section 3.1) and fluctuating features of the jump roller – namely, the dimensionless F_{toe} and F_{eddy} – showed higher values for the rough bed for the same inflow Froude number. Hence, for $Re_1 > 1.7 \times 10^5$, $F_{toe} \times d_1/V_1$ was larger than 0.022 and 0.014 on rough and smooth bed configurations, respectively.

4.2 Characteristics of impingement perimeter and free-surface profile

The hydraulic jump was most often studied in two dimensions considering a constant rate of variation of parameters in the

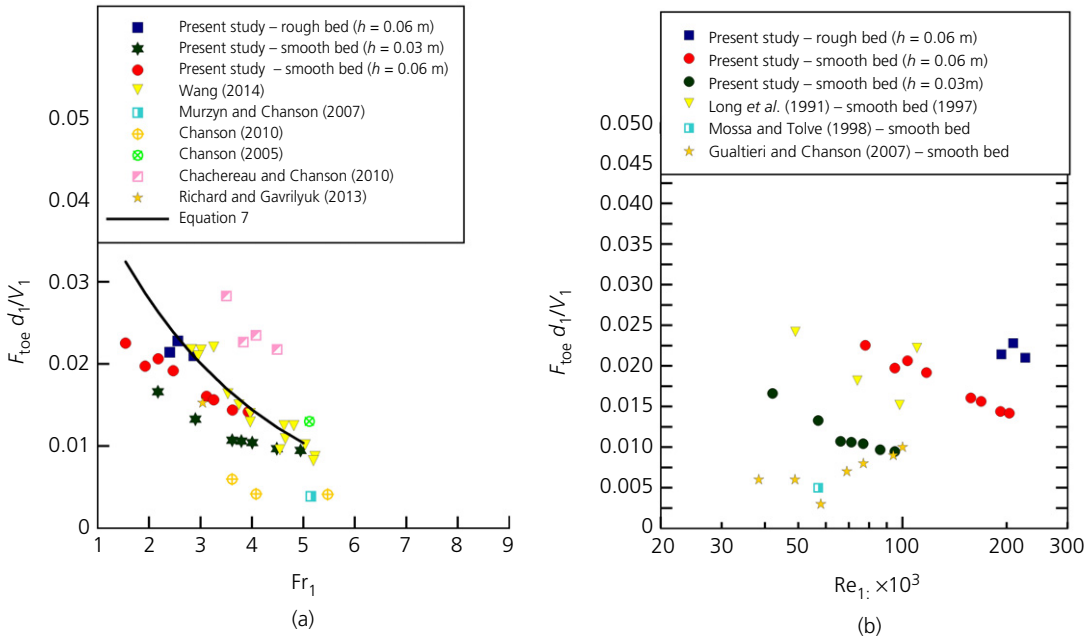

Q23 Q22 **Figure 6.** Longitudinal oscillations of the jump toe: (a) based upon inflow Froude number; (b) based upon inflow Reynolds number

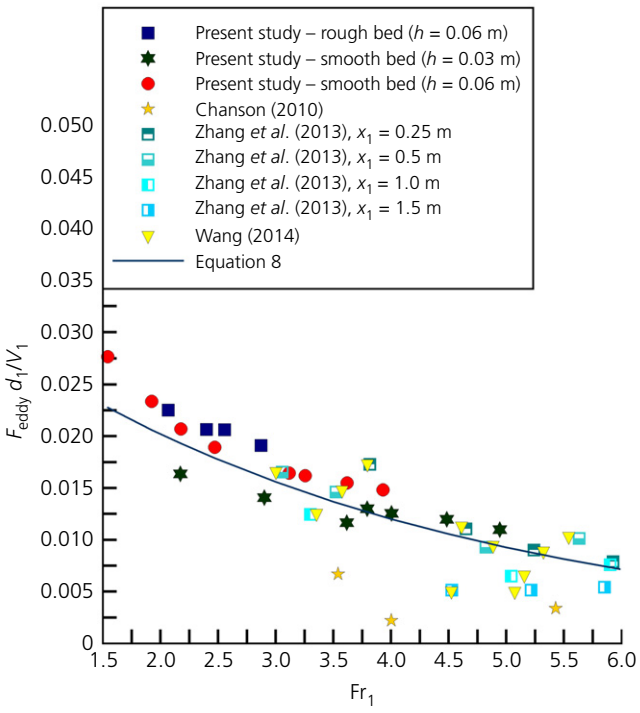

Figure 7. Frequency of large vortex ejections based upon inflow Froude number

Table 4. Experimental runs for the analysis of transverse impingement perimeter and water surface variation, $x_1 = 1$ m

Bed type	Run	Q: m^3/s	h: m	d_1: m	Fr_1	Re_1
Smooth	S1	0.08	0.06	0.062	3.25	1.7×10^5
Rough	R1	0.1	0.06	0.082	2.87	2.2×10^5
	R2	0.092		0.084	2.56	2.1×10^5
	R3	0.085		0.083	2.40	1.9×10^5

transverse direction (Chachereau and Chanson, 2011; Kucukali and Chanson, 2008, Wang, 2014; Zhang *et al.*, 2013). Transverse flow structures on a smooth bed have received little attention until recently, and no study has been reported on a rough bed. Herein, the transverse perimeter of hydraulic jump toe and the free-surface profile dynamics were investigated on both rough and smooth bed configurations. Although measurements of jump toe oscillation have traditionally been conducted by way of video camera through the sidewalls, the side views show the maximum water surface profile that could occur at any transverse position. The instantaneous impingement perimeter and free-surface profiles were measured using high-speed video. Videos were recorded for the side and overhead views at 240 frames per second for a duration of 1 min. The frames were extracted by Matlab image processing capability. Then, the jump toe perimeter and water surface profile were extracted using Plot-Digitizer software for at least 50 and 120 data points per whole width for top and side views, respectively.

From a total of 2500 continuous frames, one in five frames (500 out of 2500) was extracted to analyse both top and side views for each flow condition. Two different analyses were conducted on the profiles of the instantaneous jump toe perimeter

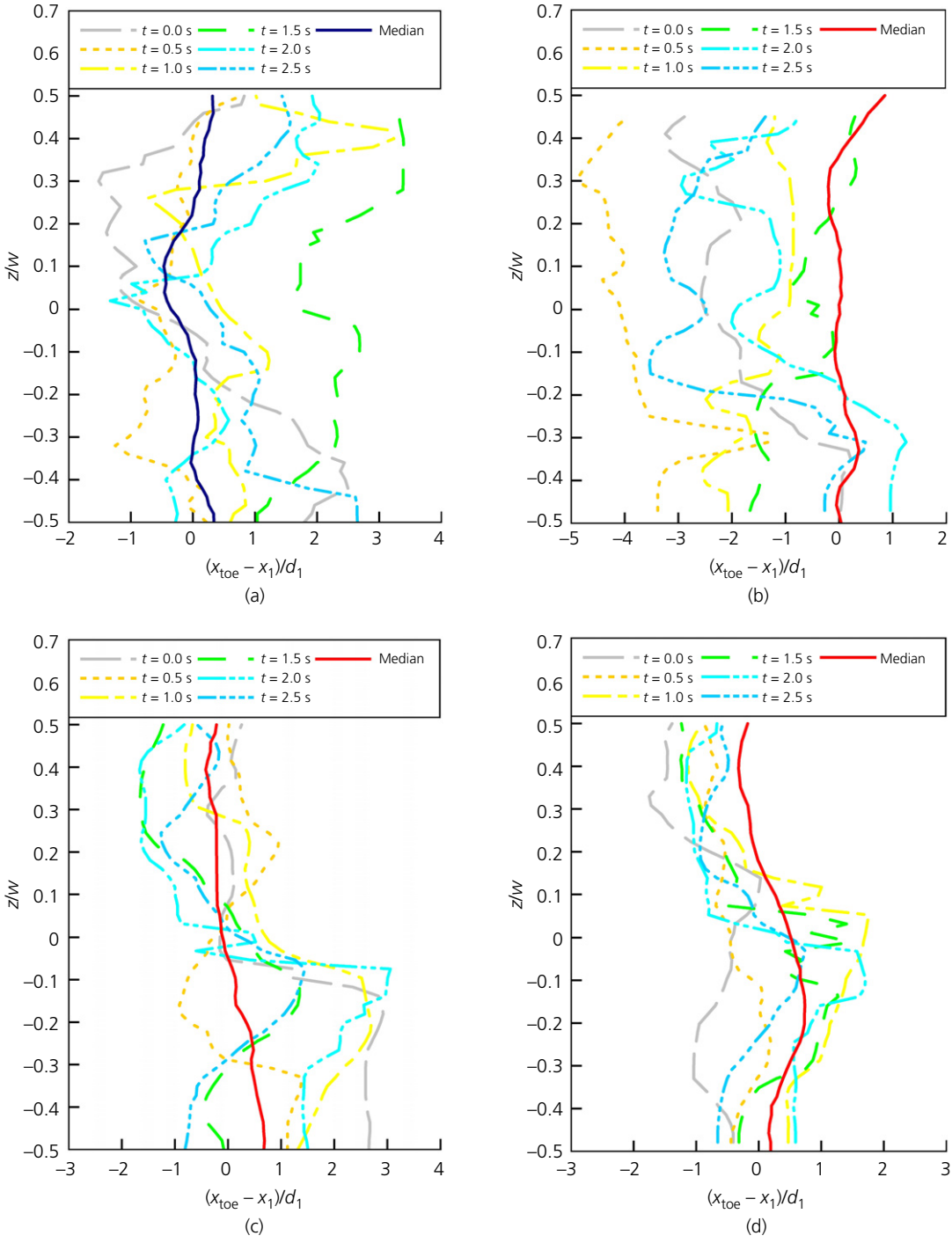

Figure 8. Analysis of six frames for jump toe perimeter. Run S1: $Q = 0.078$ m^3/s, $Fr_1 = 3.25$ for smooth bed; run R1: $Q = 0.1$ m^3/s, $Fr_1 = 2.87$; run R2: $Q = 0.092$ m^3/s, $Fr_1 = 2.56$; and run R3: $Q = 0.085$ m^3/s, $Fr_1 = 2.4$ for rough bed. With the same gate opening $h = 0.06$ m: (a) smooth bed, run S1, $Fr_1 = 3.25$; (b) rough bed, run R1, $Fr_1 = 2.87$; (c) rough bed, run R2, $Fr_1 = 2.56$; (d) rough bed, run R3, $Fr_1 = 2.4$

and free-surface data. First, six frames with a time step of 0.5 s were analysed. Second, the analysis considered all of the 500 frames in terms of the median of the impingement perimeter. For both analyses, the range of oscillations of the instantaneous data as well as their probability density function (PDF) and statistical distribution were studied. The instantaneous impingement and free-surface profiles in terms of the domain of variation, PDF and the shape of the distribution,

were analysed using the *dfittool* function of Matlab software. The flow conditions are listed in Table 4.

4.2.1 Impingement perimeter

The median impingement point position x_{toe} and the standard deviation x'_{toe} were calculated at the transverse locations z ($-0.5 \leq z/W \leq 0.5$). For all frames, the data were recorded every 1 mm in the transverse direction.

The results from the analysis of six frames are presented in Figure 8. Different shapes of the jump toe perimeter were observed (Figures 8(a) and 8(b)). The most frequently observed transverse pattern in the highly aerated hydraulic jumps was the arc-shaped perimeter bending towards downstream, as already reported by Wang (2014) on a smooth bed. Compared to the central free-stream region, the development of lateral boundary layers resulted in a lower velocity near the side-walls. Thus, on the channel centreline, the local Fr_1 was slightly larger than that next to the wall. Table 5 lists the statistical parameters of the instantaneous jump toe position. The jump toe perimeter had the largest variation at the largest Fr_1 (Table 5, Figures 8(c) and 8(d)). For $Fr_1 > 2.8$, the jump toe perimeter on a rough bed varied more than that on a smooth bed (Table 5). A larger range of fluctuations on the rough bed could be a sign of instability of the hydraulic jump (Figures 8(a) and 8(b)). For $Fr_1 = 2.56$ and 2.4 on a rough bed (Figures 8(c) and 8(d)), the asymmetrical shape of the jump toe perimeter was related to undular jump with an unstable roller condition, as well as irregularity of the jump toe oscillation (Section 3.1).

Table 5. Statistical data for the instantaneous jump toe position

Bed type	Run	$(x_{toe} - x_1)/d_1$ (six frames)	$(x_{toe} - x_1)/d_1$ (500 frames)	PDF_{max}
Rough	R1	(−3.0, 2.4)	(−3.4, 4.2)	0.3
	R2	(−3.2, 4.5)	(−3.4, 4.4)	0.23
	R3	(−1.65, 3.05)	(−1.3, 3.1)	0.53
Smooth	S1	(−1.75, 1.75)	(−3.4, 2.9)	0.42

The results of the second analysis – that is for all of the 500 frames – are shown in Figure 9. The median and the standard deviation of jump toe perimeter exhibited the same trend for both bed types, except possibly for $Fr_1 = 2.4$ on a rough bed because of the undular jump. In Figure 9(b), despite different x_1 used by Wang (2014) on a smooth bed, the standard deviation was in the same range for all of the cases. A comparison between the current data and the observations on a smooth bed by Wang (2014) highlighted that, regardless of the bed type, the transverse profile of the time-averaged jump toe perimeter was almost straight across the transverse direction at the central region of the channel ($-0.3 < z/W < 0.3$) for $Fr_1 > 2.5$ (Figure 9(b)). These findings were consistent with those of Felder and Chanson (2018) on

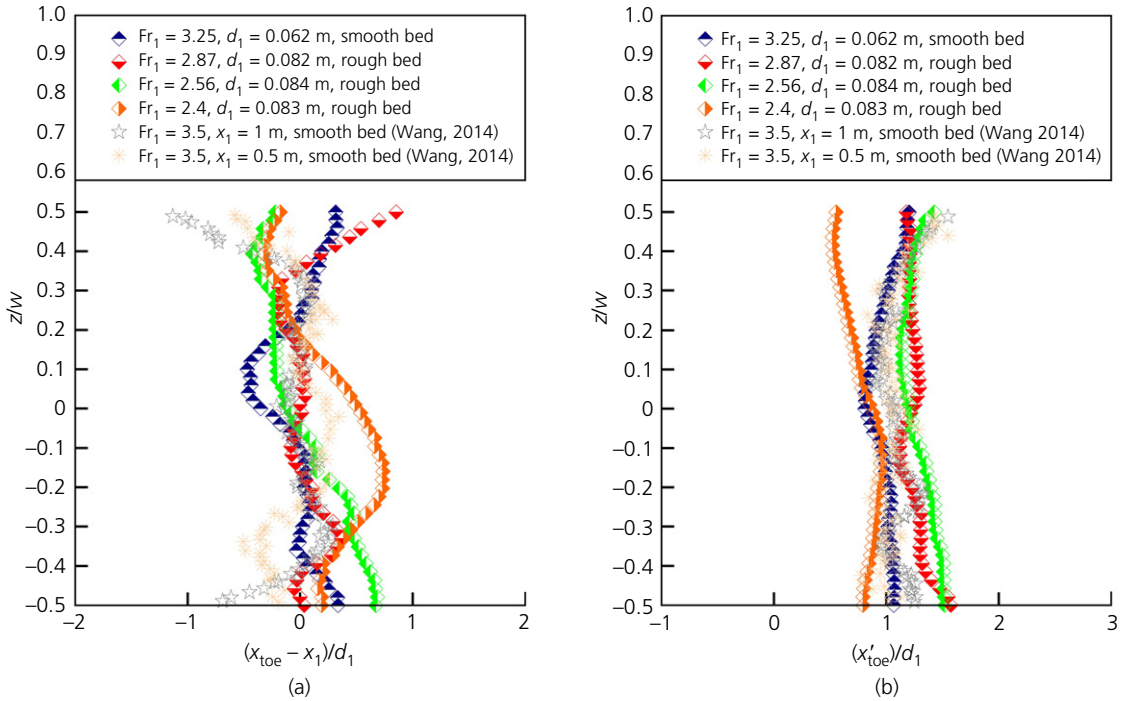

Figure 9. Characteristics of the instantaneous jump toe position through the full channel width, comparison with Wang (2014). Run R1: $Q = 0.1$ m^3/s, $Fr_1 = 2.87$; run R2: $Q = 0.092$ m^3/s, $Fr_1 = 2.56$; and run R3: $Q = 0.085$ m^3/s, $Fr_1 = 2.4$ for rough bed and run S1: $Q = 0.078$ m^3/s, $Fr_1 = 3.25$ for smooth bed. Gate opening $h = 0.06$ m: (a) median jump toe perimeter profiles; (b) standard deviation of instantaneous jump toe position

rough bed type 1 for $Fr_1 = 4.2$. For $Fr_1 > 4.2$, they pointed out large differences in terms of impingement perimeter and standard deviation with a large spread of values. For $Fr_1 = 2.4$ on a rough bed, x_{toe} and x'_{toe} had a shape different from those in the other flow conditions (Figures 9(a) and 9(b)). This might be due to the undular type of hydraulic jump with an unstable roller (Section 3.1). Regardless of the bed type, the impingement point fluctuations were almost constant across the transverse direction for each flow condition, with larger magnitude near the side-walls. The boundary-affected region near both side-walls was almost 0.1 m wide. The present data were in agreement with the Lidar observations documented by Montano *et al.* (2018) and Montano and Felder (2020) for hydraulic jump on a smooth bed. They reported the range of $0.5 < x'_{toe}/d_1 < 1.56$ for $2.1 < Fr_1 < 4.7$.

Figure 10 plots all PDFs of the instantaneous jump toe position for $Fr_1 = 2.4$, 2.56, 2.87 on a rough bed and for $Fr_1 = 3.25$ on a smooth bed for the whole width of the channel. Different types of distribution were tested by applying the Anderson–Darling statistic (Anderson and Darling, 1952). The method is based on a comparison between a given sample's empirical distribution function and the theoretical distribution, and it was described in Stephens (1974).

For a specified data set and distribution, the best data fit was obtained for the smallest Anderson–Darling statistics (Marsaglia and Marsaglia, 2004; Stephens, 1974). For the jump toe perimeter, some randomness in the fluctuation of the impingement point was suggested by the consistent relationship between the PDF and the normal distribution, as expressed by the normalised correlation coefficient. The amplitude of the oscillations of the instantaneous jump toe location around the time-averaged value was investigated using the PDF of the instantaneous jump toe location. The PDF_{max} (as the largest magnitude of PDF for each set of the data) value showed that generally the oscillation of the jump toe location was most frequently placed within the range of $-1 < (x_{toe} - x_1)/d_1 < 1$.

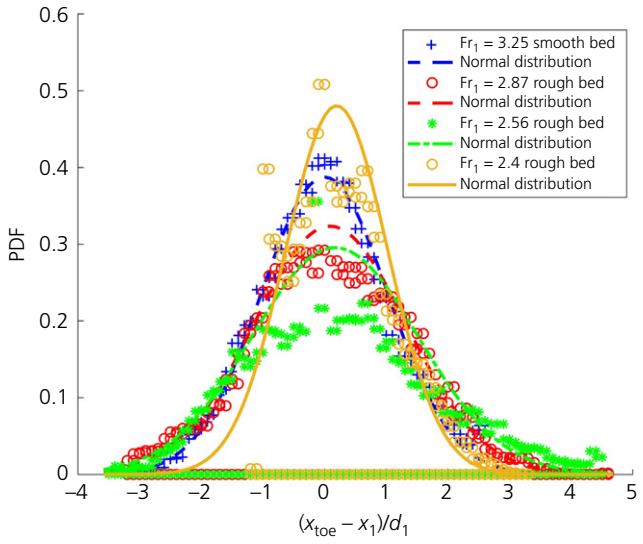

Figure 10. Probability density functions of instantaneous jump toe position; $Fr_1 = 2.87$, 2.56, 2.4 with $d_1 = 0.082$, 0.84, 0.083 m, respectively, on rough bed, $Fr_1 = 3.25$, $d_1 = 0.062$ m on smooth bed

For a hydraulic jump with stable roller – that is, $Fr_1 > 2.8$ – a broader distribution of instantaneous jump toe position was observed on a rough bed (Table 5). A larger PDF_{max} value was found on the smooth bed: $PDF_{max} = 0.42$ and 0.30 on a smooth and a rough bed, respectively (Figure 10).

For hydraulic jump with unstable roller – that is, $Fr_1 = 2.56$ and 2.4 on a rough bed – a broader distribution of the instantaneous jump toe position was observed for $Fr_1 = 2.56$ (Table 5), while PDF_{max} was 0.23 and 0.53 for $Fr_1 = 2.56$ and 2.4, respectively. The broader distribution demonstrated the larger variation of the jump toe perimeter for $Fr_1 = 2.56$, while PDF_{max} indicated that the jump toe perimeter tended to the centreline. The asymmetric shape of data distribution for $Fr_1 = 2.4$ on a rough bed was related to the asymmetric shape of the x_{toe} (Figure 10(a)). Overall, for a rough bed, the oscillations in the jump toe perimeter increased as Fr_1 increased. Regardless of Fr_1 and bed type, the data followed a normal distribution, as already reported by Wang (2014) for a smooth bed.

4.2.2 Free-surface profile

The analyses carried out on the impingement perimeter – that is the first and second method of analysis – were also repeated on the free-surface data. The local free-surface profile was recorded every 1 mm along the longitudinal direction, through the side wall.

The results from the first analysis applied to the free-surface data are presented in Figure 11 and in Table 6. Figure 11 presents the longitudinal distribution of the dimensionless elevation of the free-surface η/d_1, while Table 6 lists the data of the dimensionless change in elevation $\Delta(\eta/d_1)$.

The data showed that, at the largest Fr_1, these fluctuations were larger on a smooth bed. For $Fr_1 > 2.8$, the range of local vertical fluctuations of free-surface elevations on a smooth bed was larger than that on a rough bed (Figures 11(a) and 11(b), Table 6). At lower Fr_1 – that is, $Fr_1 = 2.4$ and 2.56 – the highest fluctuation of water surface was observed in the roller area close to the jump toe. Close to the jump toe, the range of variation for the water surface was $\Delta(\eta/d_1) = 2.04$ and 1.31 for $Fr_1 = 2.4$ and 2.56 on a rough bed, respectively. Further downstream, it was $\Delta(\eta/d_1) = 0.83$ and 0.57 for $Fr_1 = 2.4$ and 2.56 on a rough bed, respectively (Figures 11(c) and 11(d)). Overall, these findings were in agreement with undular jump with an unstable roller and irregular water surface fluctuation on a rough bed (Section 3.1).

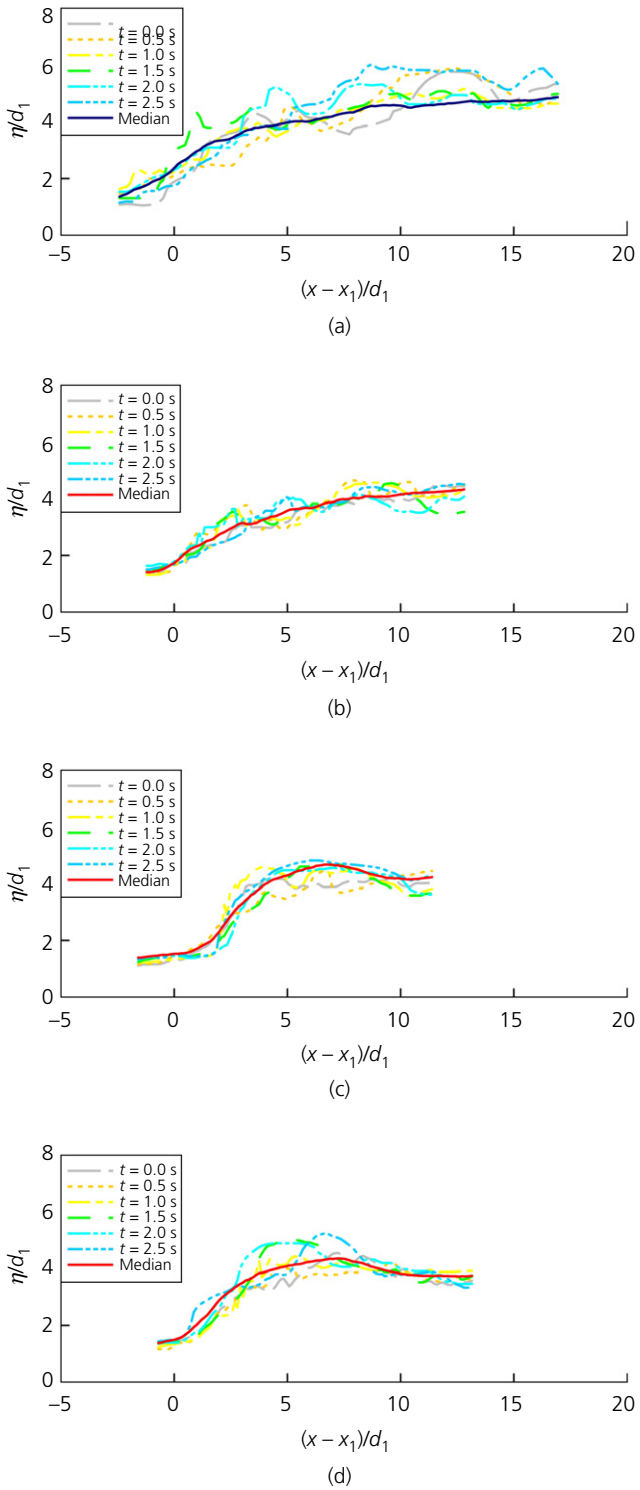

Figure 11. Continuous frames with time step of 0.5 s for longitudinal free-surface profile, run S1: $Q = 0.078$ m^3/s, $Fr_1 = 3.25$ for smooth bed; run R1: $Q = 0.1$ m^3/s, $Fr_1 = 2.87$; run R2: $Q = 0.092$ m^3/s, $Fr_1 = 2.56$; and run R3: $Q = 0.085$ m^3/s, $Fr_1 = 2.4$ for rough bed. With the same gate opening $h = 0.06$ m: (a) smooth bed, run S1, $Fr_1 = 3.25$; (b) rough bed, run R1, $Fr_1 = 2.87$; (c) rough bed, run R2, $Fr_1 = 2.56$; (d) rough bed, run R3, $Fr_1 = 2.4$

Table 6. Statistical data for the variation of free-surface profile

Bed type	Run	$\Delta(\eta/d_1)$ (six frames)	η'/d_1 (500 frames)
Rough	R1	1.10	(0.16, 0.4)
	R2	1.31	(0.09, 0.19)
	R3	2.04	(0.16, 0.4)
Smooth	S1	2.40	(0.14, 0.59)

The results of the second analysis – that is, for all 500 frames – are presented in Figure 12 and Table 6. Figure 12 shows η/d_1, while Table 6 lists the data for the standard deviation of the free-surface profile η'/d_1.

On both bed types, η/d_1 increased as the distance from the jump toe increased, while the median fluctuated in the roller length and, farther downstream, decreased (Figure 12(a)). On both bed types, η/d_1 monotonically increased regardless of Fr_1 (Figure 12(a)). Furthermore, similarly to the first method of analysis, the maximum fluctuation of the free-surface level was observed close to the jump toe (Figure 12). However, the fluctuations in water surface on a smooth bed were larger than those on a rough bed, suggesting that the latter had a stronger control effect on the flow fluctuations.

η'/d_1 had a higher range of fluctuations on a smooth bed (Figure 12(b) and Table 6). On a rough bed, the lower Fr_1 resulted in a larger range of fluctuation of free-surface level (Figure 12 and Table 6). For $Fr_1 < 2.8$ on a rough bed, although the median value of the free-surface profile was derived from the average of 10 s, the undular behaviour of the hydraulic jump along the roller length affected the free surface (Figure 12(a)).

5. Conclusion

This paper has presented the results of an experimental study of hydraulic jumps on a pebbled rough bed, which is very common in natural channels. On a rough bed, visual observations revealed that, for $1.5 < Fr_1 < 2.1$, the air entrainment started at the first undular wave crest, and slowly disappeared further downstream, while, for $2.1 < Fr_1 < 2.5$, the rate of air entrainment appeared to be stronger and large eddies were observed. For $2.5 < Fr_1 < 3.1$, some irregular surface fluctuations and stronger backward flow in the recirculation zone were observed.

The present data on the smooth bed in terms of the conjugate depth ratio were consistent with past studies, while those on the rough bed were mostly aligned with the data of Carollo *et al.* (2007) and Hughes and Flack (1984) with a similar dimensionless roughness. The literature data showed that the conjugate depth ratio decreased as the dimensionless roughness K_s/d_1 increased. For the same inflow Froude number Fr_1, the roller and aerated flow lengths were comparatively shorter on the rough bed, while the jump toe oscillations were larger than on the smooth bed. Large vortices were observed on both bed types and their rate of formation decreased as the Froude number Fr_1 increased.

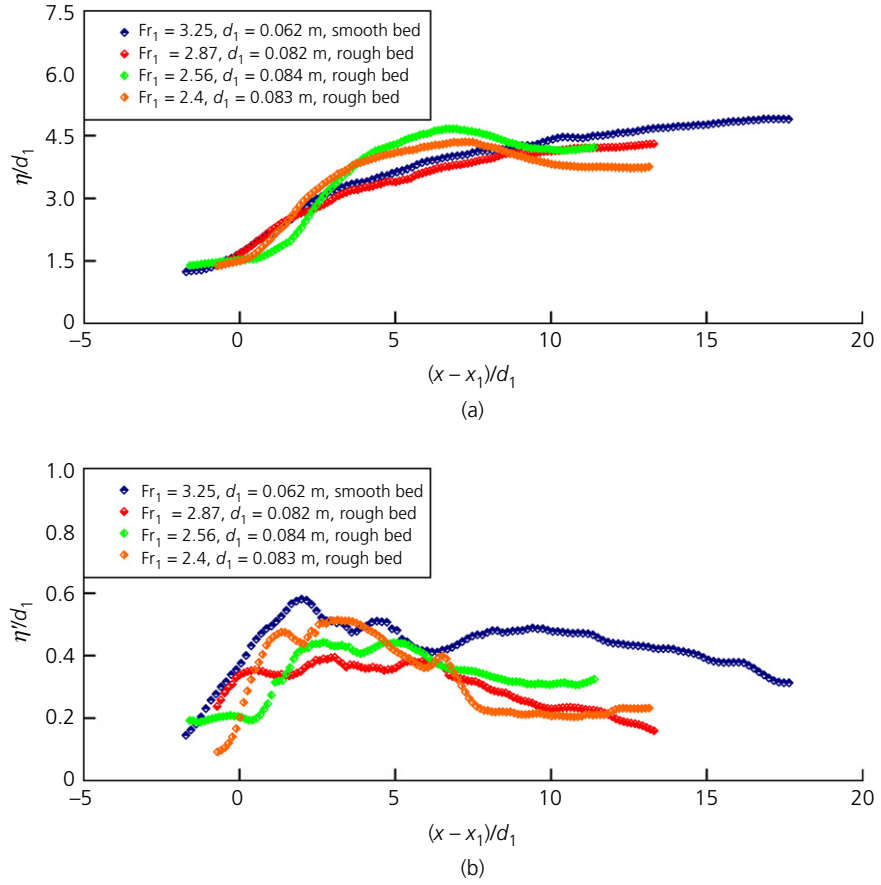

Figure 12. Median and standard deviations of the instantaneous free-surface profile through the full channel width. Run R1: $Q = 0.1$ m^3/s, $Fr_1 = 2.87$; run R2: $Q = 0.092$ m^3/s, $Fr_1 = 2.56$; and run R3: $Q = 0.085$ m^3/s, $Fr_1 = 2.4$ for rough bed; and run S1 $Q = 0.078$ m^3/s, $Fr_1 = 3.25$ on smooth bed for the same gate opening $h = 0.06$ m: (a) median free-surface profiles; (b) standard deviation of free-surface profile

On the rough bed, the jump toe perimeter had the largest variation at the largest Froude number Fr_1. The fluctuation of the longitudinal free-surface profile showed the same trend on both bed types, but the standard deviation on the smooth bed was slightly larger. The most frequently observed pattern of the impingement perimeter was the arc-shaped perimeter bending towards the downstream. The data highlighted the constant fluctuation of the impingement point across the channel, regardless of bed type. The highest fluctuation of the free-surface profile was also observed close to the jump toe. Furthermore, for the instantaneous jump toe position on both bed types, regardless of inflow Froude number, the data followed a normal distribution. The larger PDF_{max} was associated with the larger Fr_1 on a rough bed, suggesting a lower rate of fluctuation.

Overall, the study gained some novel information about the main characteristics of a hydraulic jump on a gravel bed, highlighting differences and commonalities with respect to those on a smooth bed.

Acknowledgements

The authors thank Jason Van Der Gevel and Stewart Matthews for their technical assistance (Hydraulic Laboratory of The University of Queensland). The study was conducted within the PhD Program in Civil Systems Engineering of the first author, who acknowledges the financial support from the University of Napoli Federico II.

APPENDIX 1. BOUNDARY FRICTION FORCE, SHEAR STRESS AND VORTEX ADVECTION VELOCITY

A1.1 Boundary friction force and shear stress

According to the momentum features considered for a rectangular horizontal channel, the boundary friction force could be derived as (Felder and Chanson, 2018)

$$9. \quad \frac{F_{fric}}{\rho \times g \times W \times d_1^2} = \left[\frac{Fr_1^2}{(1/2) \times (d_2/d_1)} - \left(1 + \frac{d_2}{d_1}\right)\right] \times \left(\frac{d_2}{d_1} - 1\right)$$

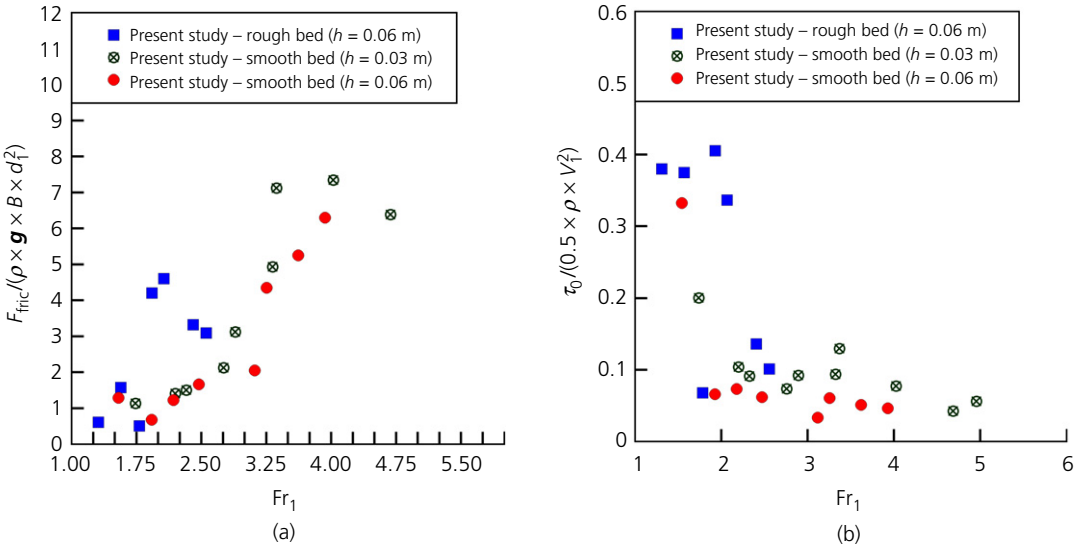

Figure 13. Boundary friction force and shear stress: (a) dimensionless boundary friction force; (b) dimensionless boundary shear stress

where W is channel width (m). Assuming the roller length based on Equation 9, the average boundary shear stress was calculated as (Felder and Chanson, 2018)

$$\frac{\tau_0}{(1/2) \times \rho \times V_1^2} = \frac{(d_2/d_1 - 1)}{3 \times Fr_1^2 \times (Fr_1 - 1)^{[1-0.64\times(K_s/d_1)]}} \times \left[\frac{Fr_1^2}{(1/2) \times (d_2/d_1)} - \left(1 + \frac{d_2}{d_1}\right)\right] \quad (10)$$

On a smooth bed, the boundary friction force increased as the inflow Froude number increased, independent of the gate opening h_1 (Figure 13), while on the rough bed the force increased for $Fr_1 < 2$ and then decreased for $Fr_1 > 2$. Overall, on the rough bed, the boundary friction force and the dimensionless average boundary shear stress were larger than on the smooth bed. For $Fr_1 > 2$, the trend of variation of boundary shear stress was the same for the smooth bed; however, at $h = 0.03$ m, values larger than those at $h = 0.06$ m were seen.

A1.2 Vortex advection velocity

Surface fluctuations were observed to propagate towards the downstream when vortical structures were formed and advected longitudinally within the roller length. Figure 14 sketches the advection of large vortices in a developing mixing layer on a smooth bed. The vortex advection velocity is denoted U_{eddy} and it was measured from the analysis of video frames recorded from the side view for different flow conditions on both bed configurations. It was measured as the average velocity of the vortices, formed at the longitudinal position of the jump toe, until they vanished in the downstream region. Figure 15 shows the distribution of the dimensionless vortex advection velocity U_{eddy}/V_1 for different Fr_1 and Re_1.

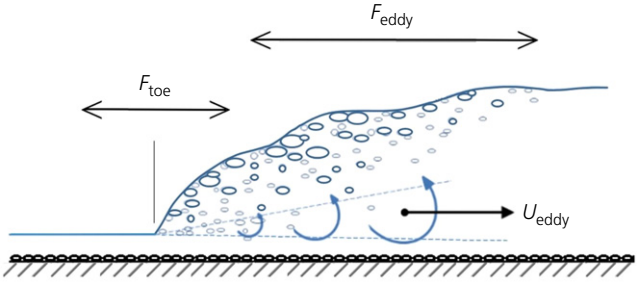

Figure 14. Sketch of large vortices advected in the turbulent shear layer on rough bed (based on Wang *et al.*, 2015)

The vortex advection velocity U_{eddy}/V_1 was almost independent of both Fr_1 and Re_1, with an average $U_{eddy}/V_1 = 0.43$ for both gates opening of a smooth bed and $U_{eddy}/V_1 = 0.46$ for a rough bed. The results were comparable to those on a smooth bed from Chanson (2010) and Wang (2014), which found a mean magnitude $U_{eddy}/V_1 = 0.32$ and 0.41, respectively.

APPENDIX 2. EXPERIMENTAL UNCERTAINTIES

The uncertainties in these experiments were related to: (*a*) the accuracy of the experimental set-up and (*b*) the accuracy of the instrumentation. The former was closely associated with the fluctuating nature of the flow. With the same flume and instrumentation, Wang (2014), based upon an experimental study of hydraulic jump on a smooth bed, stated that the Venturi meter had an accuracy of ±2% in the discharge measurement, while uncertainties up to ±8% were associated with the measurement of inflow depth due to the free-surface roughness of the impinging flow. The pointer gauge measurements were

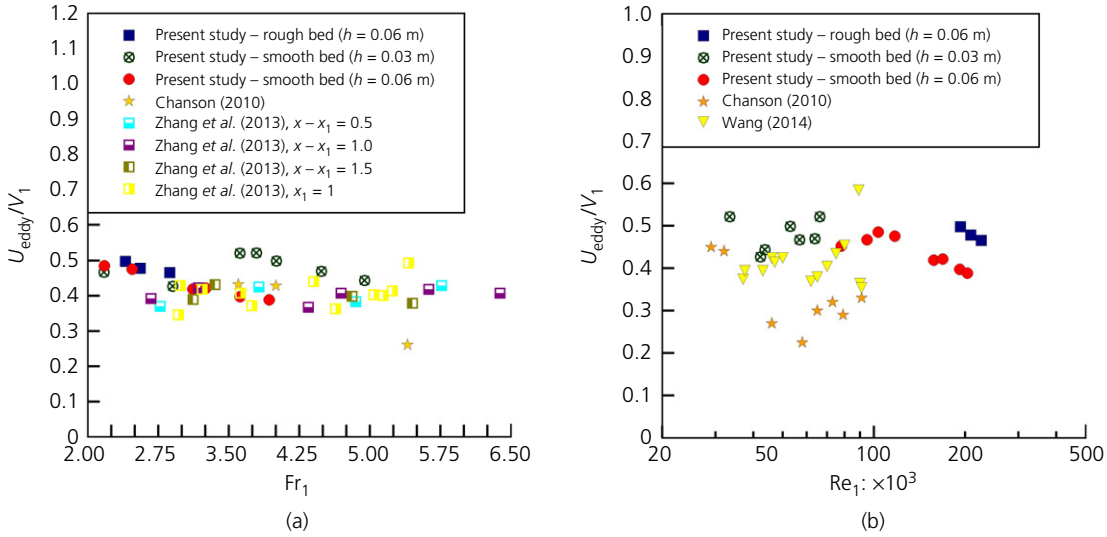

Figure 15. Advection velocity of large vortices: (a) based upon inflow Froude number; (b) based upon inflow Reynolds number

recorded for several seconds, and the mean free-surface recordings were averaged. The uncertainties of the conjugate depth d_1 were within 0.5 cm accuracy for all measured data. The largest uncertainty was associated with the visual determination of the mean longitudinal position of the oscillating jump toe. In this regard, the accuracy of the mean jump toe position was expected to be within ±0.01 m, corresponding to the largest uncertainty of ±12% for the positioning of the first longitudinal measurement location. Overall, both uncertainties in terms of inflow depth and jump toe positioning were largely affected by the turbulence level of the flow.

Note that the spikes due to instantaneous detection from camera images could result in increasing the STD magnitude for both jump toe oscillations and water surface profiles; therefore, they were considered as a part of the measurement uncertainty.

REFERENCES

Anderson TW and Darling DA (1952) Asymptotic theory of certain 'goodness of fit' criteria based on stochastic processes. *Annals of Mathematical Statistics* **23(2)**: 193–212.

Bahmanpouri F (2019) *Experimental Study of Air Entrainment in Hydraulic Jump on Pebbled Rough Bed*. PhD thesis, Civil, Architectural and Environmental Engineering Department, The University of Napoli Federico II, Naples, Italy.

Q8 Bahmanpouri F, Gualtieri C and Chanson H (2019) Air–water flow characteristics in hydraulic jump on pebbled rough bed. In *Proceedings of the 38th International Conference, IAHR World Congress, Panama City, Panama*, https://doi.org/10.3850/38WC092019-0557.

Bayon A, Valero D, García-Bartual R, Vallés-Morán FJ and López-Jiménez PA (2016) Performance assessment of OpenFOAM and FLOW-3D in the numerical modeling of a low Reynolds number hydraulic

Q9 jump. *Environmental Modelling & Software* **80**: 322–335.

Bélanger JB (1841) *Notes sur l'Hydraulique*. Ecole Royale des Ponts et Chaussées, Paris, France, 223 (in French).

Bidone G (1820) Expériences sur le remou et la propagation des ondes. *Memorie della Reale Accademia delle Scienze di Torino* **30**: 195–292. Q10

Carollo FG, Ferro V and Pampalone V (2007) Hydraulic jump on rough beds. *Journal of Hydraulic Engineering* **133(9)**: 989–999, https://doi.org/10.1061/(ASCE)0733-9429(2007)133:9(989).

Carollo FG, Ferro V and Pampalone V (2009) New solutions of classical hydraulic jump. *Journal of Hydraulic Engineering* **135(6)**: 527–531, https://doi.org/10.1061/(ASCE)HY.1943-7900.0000036.

Carollo FG, Ferro V and Pampalone V (2013) Sequent depth ratio of B-jumps on smooth and rough beds. *Journal of Agricultural Engineering* **44(2)**: 82–86, https://doi.org/10.4081/jae.2013.e12.

Chachereau Y and Chanson H (2010) *Free-surface Turbulent Fluctuations and Air–Water Flow Measurements in Hydraulic Jumps with Small Inflow Froude Numbers*. School of Civil Engineering, The University of Queensland, Brisbane, Australia, Hydraulic Model Report No. CH78/10.

Chachereau Y and Chanson H (2011) Free-surface fluctuations and turbulence in hydraulic jumps. *Experimental Thermal and Fluid Science* **35(6)**: 896–909, https://doi.org/10.1016/j.expthermflusci.2011.01.009.

Chanson H (2004) *The Hydraulics of Open Channel Flow: An Introduction*, 2nd edn. Butterworth-Heinemann, Oxford, UK.

Chanson H (2005) *Air Bubble Entrainment in Hydraulic Jumps: Similitude and Scale Effects*. Department of Civil Engineering, The University of Queensland, Brisbane, Australia, Hydraulic Model Report No. CH57/05.

Chanson H (2009) *Advective Diffusion of Air Bubbles in Hydraulic Jumps with Large Froude Numbers: An Experimental Study*. School of Civil Engineering, The University of Queensland, Brisbane, Australia, Hydraulic Model Report No. CH75/09.

Chanson H (2010) Convective transport of air bubbles in strong hydraulic jumps. *International Journal of Multiphase Flow* **36(10)**: 798–814, https://doi.org/10.1016/j.ijmultiphaseflow.2010.05.006.

Chanson H (2011) Hydraulic jumps: turbulence and air bubble entrainment. *La Houille Blanche* **2011(3)**: 5–16, doi.org/10.1051/lhb/2011026. Q11

Defina A, Susin FM and Viero DP (2008) Bed friction effects on the stability of a stationary hydraulic jump in a rectangular upward sloping channel. *Physics of Fluids* **20(3)**: 1–7, https://doi.org/10.1063/1.2841622.

Ead SA and Rajaratnam N (2002) Hydraulic jumps on corrugated beds. *Journal of Hydraulic Engineering* **128(7)**: 656–663, https://doi.org/10.1061/(ASCE)0733-9429.

Felder S and Chanson H (2016) *An Experimental Study of Air–Water Flows in Hydraulic Jumps with Channel Bed Roughness*. University of New South Wales, Sydney, Australia, WRL Research Report WRL 259.

Felder S and Chanson H (2018) Air–water flow patterns of hydraulic jumps on uniform beds macroroughness. *Journal of Hydraulic Engineering* **144(3)**: 1–12, https://doi.org/10.1061/(ASCE)HY.1943-7900.0001402.

Felder S and Pfister M (2017) Comparative analyses of phase-detective intrusive probes in high-velocity air–water flows. *International Journal of Multiphase Flow* **90**: 88–101, https://doi.org/10.1016/j.
Q12 ijmultiphaseflow.2016.12.009.

Gualtieri C and Chanson H (2007) Experimental analysis of Froude number effect on air entrainment in the hydraulic jump. *Environmental Fluid Mechanics* **7(3)**: 217–238, https://doi.org/10.1007/s10652-006-9016-1.

Gualtieri C and Chanson H (2010) Effect of Froude number on bubble clustering in a hydraulic jump. *Journal of Hydraulic Research* **48(4)**: 504–508, https://doi.org/10.1080/00221686.2010.491688.

Gualtieri C and Chanson H (2013) Interparticle arrival time analysis of bubble distributions in a dropshaft and hydraulic jump. *Journal of Hydraulic Research* **51(3)**: 253–264, https://doi.org/10.1080/00221686.2012.762430.

Hager WH and Bremen R (1989) Classical hydraulic jump: sequent depths. *Journal of Hydraulic Research* **27(5)**: 565–585, https://doi.org/10.1080/00221688909499111.

Hager WH, Bremen R and Kawagoshi N (1990) Classical hydraulic jump: length of roller. *Journal of Hydraulic Research* **28(5)**: 591–608.

Hoyt JW and Sellin RHJ (1989) Hydraulic jump as 'mixing layer'. *Journal of Hydraulic Engineering* **115(12)**: 1607–1614.

Hughes WC and Flack JE (1984) Hydraulic jump properties over a rough bed. *Journal of Hydraulic Engineering* **110(12)**: 1755–1771, https://doi.org/10.1061/(ASCE)0733-9429(1984)110:12(1755).

Kucukali S and Chanson H (2008) Turbulence measurements in hydraulic jumps with partially-developed inflow conditions. *Experimental Thermal and Fluid Science* **33(1)**: 41–53.

Lennon JM and Hill DF (2006) Particle image velocity measurements of undular and hydraulic jumps. *Journal of Hydraulic Engineering* **132(12)**: 1283–1294, https://doi.org/10.1061/(ASCE)0733-9429(2006)132:12(1283).

Li Y and Chanson H (2018) Decelerating bores in channels and estuaries. *Coastal Engineering Journal* **60(4)**: 449–465, https://doi.org/10.1080/21664250.2018.1529261.

Long D, Steffler P and Rajaratnam N (1991) A numerical study of submerged hydraulic jumps. *Journal of Hydraulic Research* **29(3)**: 293–308, https://doi.org/10.1080/00221689109498435.

Marsaglia G and Marsaglia J (2004) Evaluating the Anderson–Darling distribution. *Journal of Statistical Software* **9(2)**: 1–5, http://hdl.handle.net/10.18637/jss.v009.i02.

Montano L and Felder S (2020) LIDAR observations of free-surface time and length scales in hydraulic jumps. *Journal of Hydraulic Engineering* **146(2020)**: 04020007.

Montano L, Li R and Felder S (2018) Continuous measurements of time-varying free-surface profiles in aerated hydraulic jumps with a LIDAR. *Experimental Thermal and Fluid Science* **93(2018)**: 379–397.

Montes SJ (1998) *Hydraulics of Open Channel Flow*. ASCE Press, New York, NY, USA.

Mortazavi M, Chenadec V, Moin P and Mani A (2016) Direct numerical simulation of a turbulent hydraulic jump: turbulence statistics and air entrainment. *Journal of Fluid Mechanics* **797**: 60–94. Q15

Mossa M and Tolve U (1998) Flow visualization in bubbly two-phase hydraulic jump. *Journal of Fluids Engineering* **120(1)**: 160–165, https://doi.org/10.1115/1.2819641.

Mouaze D, Murzyn F and Chaplin JR (2005) Free surface length scale estimation in hydraulic jumps. *ASME Journal of Fluids Engineering* **127(6)**: 1191–1193, https://doi.org/10.1115/1.2060736.

Murzyn F and Chanson H (2007) Free surface, bubbly flow and turbulence measurements in hydraulic jumps. Hydraulic model report, No. CH63/07, Division of Civil Engineering, The University of Queenslsnd, Brisbane, Australia, 100 pages.

Murzyn F and Chanson H (2009) Experimental investigation of bubbly flow and turbulence in hydraulic jumps. *Environmental Fluid Mechanics* **9(2)**: 143–159, https://doi.org/10.1007/s10652-008-9077-4.

Murzyn F, Mouaze D and Chaplin JR (2007) Air–water interface dynamic and free surface features in hydraulic jumps. *Journal of Hydraulic Research* **45(5)**: 679–685, https://doi.org/10.1080/00221686.2007.9521804.

Pagliara S and Palermo M (2015) Hydraulic jumps on rough and smooth beds: aggregate approach for horizontal and adverse-sloped beds. *Journal of Hydraulic Research* **53(2)**: 243–252, https://doi.org/10.1080/00221686.2015.1017778.

Pagliara S, Lotti I and Palermo M (2008) Hydraulic jumps on rough bed of stream rehabilitation structures. *Journal of Hydro-environment Research* **2(1)**: 29–38, https://doi.org/10.1016/j.jher.2008.06.001.

Pagliara S, Roshni T and Carnacina I (2011) Turbulence, aeration and bubble features of air–water flows over macro- and intermediate roughness. *Water Science Engineering* **4(2)**: 170–184, https://doi.org/10.3882/j.issn.1674-2370.2011.02.005.

Rajaratnam N (1967) *Hydraulic Jumps: Advances in Hydroscience*. Academic Press, New York, NY, USA.

Rao NSL and Kobus HE (1971) *Characteristics of Self-Aerated Free-Surface Flows. Water and Waste Water/Current Research and Practice, 10*. Eric Schmidt Verlag, Berlin, Germany. Q16

Richard GL and Gavrilyuk SL (2013) The classical hydraulic jump in a model of shear shallow-water flows. *Journal of Fluid Mechanic* **725**: 492–521, https://doi.org/10.1017/jfm.2013.174. Q17

Stephens MA (1974) EDF statistics for goodness of fit and some comparisons. *Journal of American Statistical Association* **69(347)**: 730–737, https://doi.org/10.1080/01621459.1974.10480196.

Takahashi M and Ohtsu I (2017) Effects of inflows on air entrainment in hydraulic jumps below a gate. *Journal of Hydraulic Research* **2017(55)**: 259–268.

Wang H (2014) *Turbulence and Air Entrainment in Hydraulic Jumps*. Doctoral dissertation, School of Civil Engineering, The University of Queensland, Brisbane, Australia.

Wang H and Chanson H (2015) Air entrainment and turbulent fluctuations in hydraulic jumps. *Urban Water Journal* **12(6)**: 502–518, https://doi.org/10.1080/1573062X.2013.847464.

Wang H and Chanson H (2016) Self-similarity and scale effects in physical modelling of hydraulic jump roller dynamics, air entrainment and turbulent scales. *Environmental Fluid Mechanic* **16(6)**: 1087–1110, https://doi.org/10.1007/s10652-016-9466-z.

Wang H, Murzyn F and Chanson H (2015) Interaction between free-surface, two-phase flow and total pressure in hydraulic jump.

Experimental Thermal and Fluid Science **64**: 30–41, https://doi.org/10.1016/j.expthermflusci.2015.02.003.

Witt A, Gulliver JS and Shen L (2018) Numerical investigation of vorticity and bubble clustering in an air entraining hydraulic jump. *Computers & Fluids* **172**: 162–180.

Zhang G, Wang H and Chanson H (2013) Turbulence and aeration in hydraulic jumps: free-surface fluctuation and integral turbulent scale measurements. *Environmental Fluid Mechanic* **13(2)**: 189–204, https://doi.org/10.1007/s10652-012-9254-3.